



Photovoltaic Integration in Urban Environmental Design: A Sustainable Method to Energy Harvesting and Aesthetic Enhancement

Guangyu Yang*[‡], Shilong Xu**

*School of Art, Dezhou University, Dezhou City, Shandong Province, 253023, China

**School of Art and Design, Kaili University, Kaili City, Guizhou Province, 556011, China

(yangguangyu1973@126.com, xushilong94@163.com)

[‡] Corresponding Author; Guangyu YANG, xushilong94@163.com

Received: 23.11.2025 Accepted: 29.04.2026

Abstract-The long-standing separation of energy systems and visual aesthetics in current urban environmental design makes it difficult to achieve a unity of function and aesthetics in the spatial composition of photovoltaic (PV) facilities. This paper proposes a Photovoltaic Aesthetic Integration Design Method (PAIDM) based on dynamic light energy mapping and multi-objective optimization. A high-precision radiative transfer simulation of solar flux is performed by establishing a spatial distribution model of light intensity. A multi-objective genetic algorithm (MOGA) is applied to achieve the global optimization of the spatial layout and tilt angle of the components with power generation efficiency, surface reflectivity uniformity, and visual coherence as joint objectives. This study utilizes a pure simulation approach to validate the proposed algorithmic design framework. In order to maintain equilibrium between energy conversion and color coordination in the PV system, a spectral sensing mapping function is built concurrently to correct the material reflectivity characteristics. The annual average irradiance of the meridional wall is reported to be 438.6 W/m² from the experiments, which is equivalent to an energy density of 763.2 kWh/(m²·year). The visual consistency score of the single-crystalline silicon material improved from 0.68 to 0.86 after spectral correction. With the help of this study, photovoltaic integration in urban design has been redefined as the use of an active rather than a passive component for generating sustainable urbanism, where aesthetic and energy-saving can still be maintained.

Keywords Photovoltaic aesthetic integration, multi-objective genetic optimization, spectral perception mapping, urban environmental design, energy-aesthetic coupling.

1. Introduction

Urban environmental design is, therefore, an essential means to carry out the integration and innovation of renewable energy forms in the face of global carbon neutrality and energy transition. Photovoltaic (PV) energy production, which is a source of energy that is effective, clean, and eco-friendly, is considered to be the most likely to lead to the urban energy system of the future [1], [2], [3], [4]. Nonetheless, contemporary PV systems are primarily standalone or ancillary structures placed within the built environment, leading to a lack of coordination between energy systems and urban aesthetics [5], [6], [7]. Structural conflict between form priority and performance priority presents one aspect of that disconnection. For the latter, surface continuity, color

harmony, and material order are prioritized, whereas the former seeks to maximize irradiance capture and energy generation. Attaining some measure of optimization might in part be achievable through scheme selection, but scheme selection generally occupies a local optimization situation, rather than a system-level synergy, which is in part facilitated because there is no shared measure or constraint on measurement coordinates and spatial features within the same structure for both priorities. The opportunity for a combined optimization of energy performance and urban aesthetics is an important issue in sustainable design [8], [9], [10]. Consideration of PV technology design integration within buildings and the environment matters not only for energy generation performance but also for cultural expression and spatial quality in the urban landscape [11], [12], [13]. Research emphasis has shifted from performance

improvement toward rethinking relationships in order to arrive at aesthetic expressions of energy generation performance in terms of design boundaries.

The major problem with photovoltaic integrated design today is the lack of a well-defined coupling mechanism for technical performance and visual appearance. The primary contributions of this research rest in the formulation of a dynamic spatial irradiance matrix to map urban solar flux and the construction of a joint multi-objective optimization framework targeting tilt angle and spatial layout. A spectral perception mapping function is formulated to bridge the physical reflectance properties of materials with human visual sensitivity thresholds. The proposed methodology synchronously resolves the isolated treatment of geometric energy maximization and surface aesthetic coherence within a unified multi-dimensional variable space. The amount of energy produced by building-integrated photovoltaic devices can be greatly influenced by the orientation or tilt of the building surfaces, shading and reflection characteristics of the surfaces, and even the angular rise and fall of the sun in the sky [14], [15], [16]. Also, the nonuniform distribution of light makes it difficult to place the modules in such a way that there is a balance of both energy absorption and aesthetic coherence [17], [18]. Developed parametric models predominantly consider geometric optimization of the form factor or ratio of the module in terms of potential energy returns, while dynamic lighting and visual perception were often unfocused upon, and thus may lead to excessive reflections and/or the phenomenon of jarring colors [19], [20]. The absence of a simultaneous optimization mechanism of light energy properties and visual characteristics is the driving force behind the very real implications of balancing energy and aesthetics [21], [22]. Conventional methods treat module placement and visual design as sequential tasks, resulting in sub-optimal system-level performance. Maximizing form factors exclusively for irradiance causes severe surface fragmentation and visual glare. Prioritizing material uniformity without radiation constraints severely degrades the cumulative active energy harvest. The proposed methodology directly targets the missing deterministic numerical link between structural energy efficiency and spectral color harmony. The solution requires describing the intrinsic relationship between the energy field and the visual field through coupling, and achieving a unified output of parameters, objectives, and evaluations through fusion, thereby establishing a clear logical starting point for subsequent modeling and verification methods.

Current literature addressing this domain falls into distinct thematic categories regarding energy-driven optimization, perceptual aesthetic assessments, urban-scale irradiance modeling, and multi-objective algorithmic implementations. Building-integrated photovoltaic design merges structure and power generation functions. Maghrabie HM et al. systematically analyzed the energy consumption and thermal comfort effects of roof and facade BIPV systems [23]. Azami A et al. used parametric methods to establish a shape and photovoltaic area balance model and determined the optimal shape factor with the roof as the main component [24]. However, this method still has a contradiction between light energy utilization and surface consistency. Some scholars

have applied a geometric optimization strategy based on a genetic algorithm (GA) to improve light utilization by adjusting the tilt angle of photovoltaic panels. Khan AY et al. combined Computational Fluid Dynamics (CFD) simulation with a genetic algorithm to optimize the tilt angle and row spacing of roof photovoltaic arrays, and the performance ratio remained above 80% [25]. Gabriel Espitia-Mesa et al. improved the light capture by combining a genetic algorithm with ray tracing tools [26]. Recent computational frameworks validate genetic layout optimizations entirely through simulated twin environments, bypassing initial physical prototyping. However, this type of method lacks visual parameter constraints and is prone to causing appearance fragmentation. Another type of research uses parametric modeling and radiation simulation tools, such as Radiance or Ladybug, to visualize and analyze the light distribution. Masoud Valinejadshoubi et al. used Grasshopper parametric modeling combined with EnergyPlus/Honeybee energy consumption simulation and Galapagos optimization algorithm to simulate and optimize dynamic photovoltaic facades, significantly reducing energy consumption and improving lighting comfort [27]. Although the accuracy of local energy distribution has been improved, a global optimization model coupled with aesthetic indicators has not been formed. Energy-driven studies omit perceptual metrics entirely. Aesthetic research lacks quantitative validation against actual power generation yields. Newly proposed coupling metrics attempt to quantify visual glare alongside energy density, yet face scalability challenges when applied to dynamic district-level models due to exponential computational costs. Urban-scale models isolate radiation mapping from architectural design variables. Algorithmic approaches fail to incorporate spectral human response functions into their fitness evaluations. Existing research is mostly limited to the single goal of improving energy efficiency or controlling surface form, and a unified light energy-visual joint optimization mechanism has not yet been established, making it difficult for photovoltaic systems to achieve structural coordination and aesthetic integration in urban spaces. Recent scalable urban energy workflows emphasize the necessity of complementary metrics and highlight the severe computational cost challenges when expanding models to district levels [28]. Benchmarking studies evaluating simulation fidelity against measured data underscore the critical importance of physical experimental validation in building integrated photovoltaics [29].

To address the insufficient coupling between energy and visual features in photovoltaic integration, this paper proposes a Photovoltaic Aesthetic Integration Design Method (PAIDM) based on dynamic energy mapping and multi-objective optimization. The method first completes dynamic modeling of the urban lighting environment and irradiance simulation, then conducts multi-objective genetic optimization oriented towards energy-aesthetic synergy, followed by material visual correction based on spectral perception mapping, and finally constructs an energy-aesthetic integrated performance output model to form a reusable evaluation and decision-making path. In this study, the energy field and visual field are modeled simultaneously in the same variable space, and evaluation functions and constraints act simultaneously on the

geometric, optical, and perceptual levels, transcending the boundaries of single-domain optimization. Basically, layout optimization through the use of the reflectance gradient and brightness variance of the target set is a step that essentially includes visual quality measures, thereby making visual harmony a metric instead of a design preference. Spectral perception mapping, by aligning the reflectance spectrum of the material with the visual response of the human eye, gives color stability results that go hand in hand with energy efficiency, thus resulting in a closed-loop convergence chain from radiative input to aesthetic output; The VCS thresholds are derived from International Commission on Illumination glare standards. Higher indices represent alignment with human visual comfort zones. In this way, it is possible to provide a sustainable urban environmental design context that combines energy efficiency and built aesthetic value by executing an algorithmically-driven design mechanism to change a photovoltaic component from merely a useful add-on to be a built characteristic with visual beauty. This algorithmic mechanism transforms photovoltaic modules into visually integrated architectural elements. A sustainable urban design context merging energy efficiency with aesthetic value is established.

2. A Photovoltaic Aesthetic Integration Design Method Based on Dynamic Light Energy Mapping and Multi-Objective Optimization

2.1. Dynamic Modeling and Irradiance Simulation of Urban Light Environment

The method uses urban-scale 3D geometries and meteorological time series as input, builds an irradiance simulation link with direct, diffuse, and surface reflection channels, and gives a standardized spatiotemporal irradiance matrix as output. In urban bottleneck areas and high-shading street valleys, radiative transfer solution and shading projection are operated in tandem to ensure the continuity of irradiance in both spatial and temporal domains. The model is based on high-resolution three-dimensional urban building geometry data and realizes the quantification of solar flux of different surfaces under temporal changes through radiative transfer calculation and spatial projection analysis [30]. The input data includes the building surface grid coordinate set $S(x_i, y_i, z_i)$ and solar radiation intensity sequence I_t , with a sampling time interval of 1 hour, and the time scale covers the annual sunshine cycle. In order to improve the calculation accuracy, the angle between the solar position angle and the surface normal vector is calculated by spatial vector

projection, considering atmospheric scattering, albedo, and shading effect between building groups, and forming a dynamic mapping matrix of light energy through temporal superposition [31]. Light intensity is calculated using the fundamental form of the radiative transfer equation. The incoming light intensity at any location (x, y) on the building facade is called $L(x, y, t)$, and it is made up of these three components: direct solar radiation, diffuse radiation, and ground-reflected radiation. The mathematical expression of this is given in equation (1):

$$L(x, y, t) = I_t \cdot \cos(\theta_i) \cdot \tau_a \cdot \rho_s \cdot R(x, y, t) \quad (1)$$

In equation (1), τ_a signifies the atmospheric transmittance; θ_i denotes the incident angle; ρ_s refers to the building surface reflectance; and $R(x, y, t)$ denotes the radiation attenuation factor due to the shading of the building generated by the surrounding buildings. This equation applies a time variable t in the calculation of light energy distribution to reflect the dynamic changes under different solar conditions. The model uses the ray tracing method to calculate the shading projection area and realizes the continuous distribution mapping of light energy in the building group space through matrix superposition [32]. In order to ensure the stability and temporal continuity of the model on the spatial scale, the annual light data is standardized and statistically smoothed, and the standardized form of the light intensity matrix $L_m(x, y, t)$ is defined as follows:

$$L_m(x, y, t) = \frac{L(x, y, t) - L_{\min}}{L_{\max} - L_{\min}} \quad (2)$$

In equation (2), the terms L_{\max} and L_{\min} denote the maximum and minimum light intensity values in the sample set, respectively. After normalization, the light intensity matrix is spread over the 0–1 range; thus, it becomes a standardized input scale for further genetic optimization algorithms. In the data processing stage, the light intensity matrix is mapped and fused with the surface normal vector field of the 3D model to generate a surface unit dataset with spatial light intensity attributes. This dataset is used to characterize the light energy absorption potential and radiation differences of various areas of the building facade at different times, providing accurate input for the parameter optimization of photovoltaic modules. The model output is presented in the form of a light energy distribution cloud map and a light intensity statistics table, showing the light differences under different building orientations, materials, and shading conditions. As shown in Fig. 1, the dynamic light energy mapping framework embodies the entire process from radiation input to spatial light intensity output.

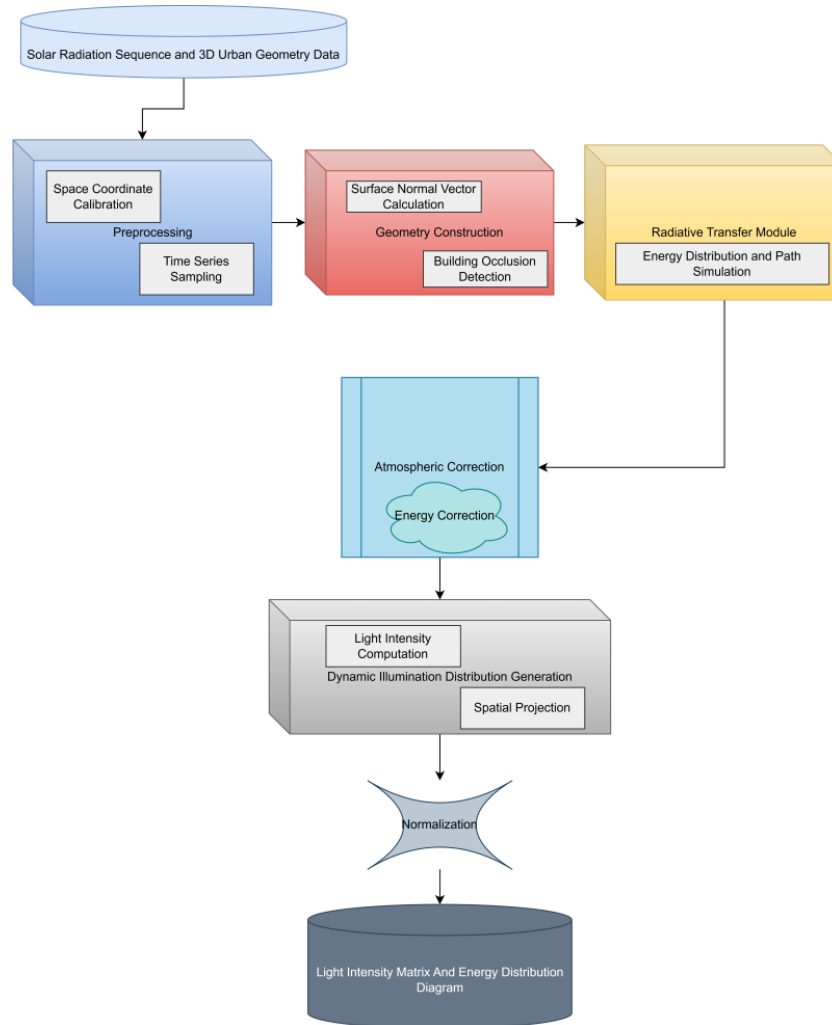


Fig. 1. Framework diagram of dynamic optical energy mapping.

The system accepts solar radiation sequences and 3D urban geometric data. For data preprocessing, spatial coordinates calibration, and time-series sampling were applied. In the building geometry construction stage, a surface normal vector calculation and shading detection were performed. In the radiation transmission module, the energy distribution and path simulation of the energy flow of direct light, diffuse light, and reflected light were performed. The atmospheric correction stage corrected for energy scattering and absorption factors. The spatial projection and light

intensity calculation module produced a dynamic lighting distribution on the building surface. The final light intensity matrix and energy distribution map were normalized, providing a data foundation as a basis for potentials for photovoltaic (PV) module layout optimization and visual coordination analysis later.

To ensure the accuracy of the lighting mapping results, the main parameters of the building surface lighting model are shown in Table 1.

Table 1. Input parameters for building surface illumination modeling

Parameter Category	Parameter Name	Unit	Assigned Value / Range	Description
Solar Radiation Model	Direct Normal Irradiance	W/m ²	200–1000	Hourly radiation input from station data
	Diffuse Horizontal Irradiance	W/m ²	50–250	Sky-scattered component input
Geometric Configuration	Surface Azimuth Angle	°	0–360	Relative orientation of building façade
	Surface Tilt Angle	°	0–90	Vertical to horizontal transition parameter

	Shading Coefficient	—	0–1	Ratio of occluded irradiance area
Temporal Resolution	Simulation Time Step	h	1	Hourly temporal sampling interval
Output Variable	Computed Irradiance Matrix	W/m ²	—	Spatial irradiance distribution matrix output

Direct normal irradiance is set at 200–1000 W/m² to reflect the fluctuations in radiation intensity under different climates and solar altitude angles; diffuse horizontal irradiance is set at 50–250 W/m² to characterize the energy contribution of atmospheric scattering and cloud reflection. Among the geometric parameters, azimuth angles of 0–360° correspond to the differences in light received by the building facade, and tilt angles of 0–90° describe the structural changes from the facade to the roof. The shading coefficient of 0–1 reflects the attenuation of incident light energy by building density; higher values indicate more areas of low local irradiance. The time step is set to 1 hour to ensure the temporal continuity of radiation variations. These parameters together constitute the core input for light energy distribution modeling, providing a stable data foundation for energy efficiency analysis and visual mapping.

2.2. Multi-objective Genetic Optimization for the Synergy Between Energy Performance and Aesthetics

After obtaining the spatial distribution matrix of light intensity, a multi-objective genetic optimization solution mechanism needs to be established for the three joint indicators of power generation efficiency, reflection balance, and visual coherence under the joint drive of the irradiance matrix and surface grid coordinates, so that energy and aesthetic indicators form a controllable trade-off in the evolution process. The multi-objective genetic optimization algorithm (MOGA) is the core solution mechanism at this stage, and its optimization objectives cover three types of indicators: power generation efficiency, reflection balance, and visual coherence [33], [34]. The optimization stage employs the non-dominated sorting approach to establish a Pareto front. Individual selection from the result set occurs during a separate decision-making phase where scalar weights determine the final configuration. The algorithm input is the light intensity matrix $L_m(x,y,t)$ and the set of grid coordinates on the building surface $S(x_i,y_i,z_i)$. Through multi-dimensional parameter encoding and fitness evolution mechanism, photovoltaic module configuration schemes that meet different performance constraints are generated. The power generation efficiency function of photovoltaic modules is defined as the annual average power generation per unit area. The calculation integrates energy values adjusted for radiation absorptivity and the incident angle cosine derived from the light intensity matrix. Its formula is given as follows in equation (3). The yield calculation incorporates the Nominal Operating Cell Temperature model to adjust for thermal degradation of module efficiency. System losses from inverter conversion and partial shading factors modify the total output. Standard metrics Performance Ratio and specific yield serve as validation indicators.

$$E = \frac{1}{A \cdot T} \int_0^T \int_A \eta(\theta_i) \cdot L_m(x,y,t) dA dt \quad (3)$$

In equation (3), A signifies the surface area of the module, E stands for average power generation efficiency, T denotes the annual sampling time length, and $\eta(\theta_i)$ denotes the energy absorption efficiency after incident angle correction. The equation employs integral form to weight and sum the annual illumination conditions, thus being able to represent the overall energy efficiency performance of the different spatial orientations. Reflection uniformity index R_b and visual coherence index V_c are used to measure the visual harmony of the photovoltaic array on the building facade. Reflection uniformity is used to describe the difference in light reflection intensity between adjacent modules, and its definition is as shown in equation (4):

$$R_b = 1 - \frac{1}{N-1} \sum_{i=1}^{N-1} \frac{|R_i - R_{i+1}|}{R_{max}} \quad (4)$$

In equation (4), R_i is the average reflectance of the i -th component; R_{max} is the maximum reflectance of the sample set; and N is the number of components. The visual coherence index is calculated through spatial gradient and color balance, using the surface brightness distribution gradient of the components as input to quantify their visual continuity on the building facade, as shown in equation (5):

$$V_c = 1 - \frac{\sum_{i=1}^N |\nabla L_i|}{\sum_{i=1}^N L_i} \quad (5)$$

In equation (5), $|\nabla L_i|$ is the magnitude of the light intensity gradient, reflecting the rate of change in brightness. A higher V_c value means that the photovoltaic array has better visual balance in spatial distribution. The MOGA algorithm uses (E, R_b, V_c) as a multi-objective function vector and a population evolution strategy to achieve non-dominated solution search in the three-dimensional target space. The gene encoding of an individual consists of three-dimensional parameters of component tilt angle, azimuth angle, and deployment position. The crossover probability is set to 0.8, the mutation probability is set to 0.15, the number of iterations is set to 500, and Pareto sorting and crowding distance are used to control the diversity of solutions. During the convergence process, the algorithm gradually forms a Pareto front for energy and visual targets to achieve dynamic trade-offs between different targets. Power generation efficiency and reflection balance show a complementary relationship in the iteration. In the early solution concentration, energy increases significantly while visual balance fluctuates greatly. After about 350 generations, it tends to stabilize. The distribution of the results of the MOGA optimization process is shown in Fig. 2.

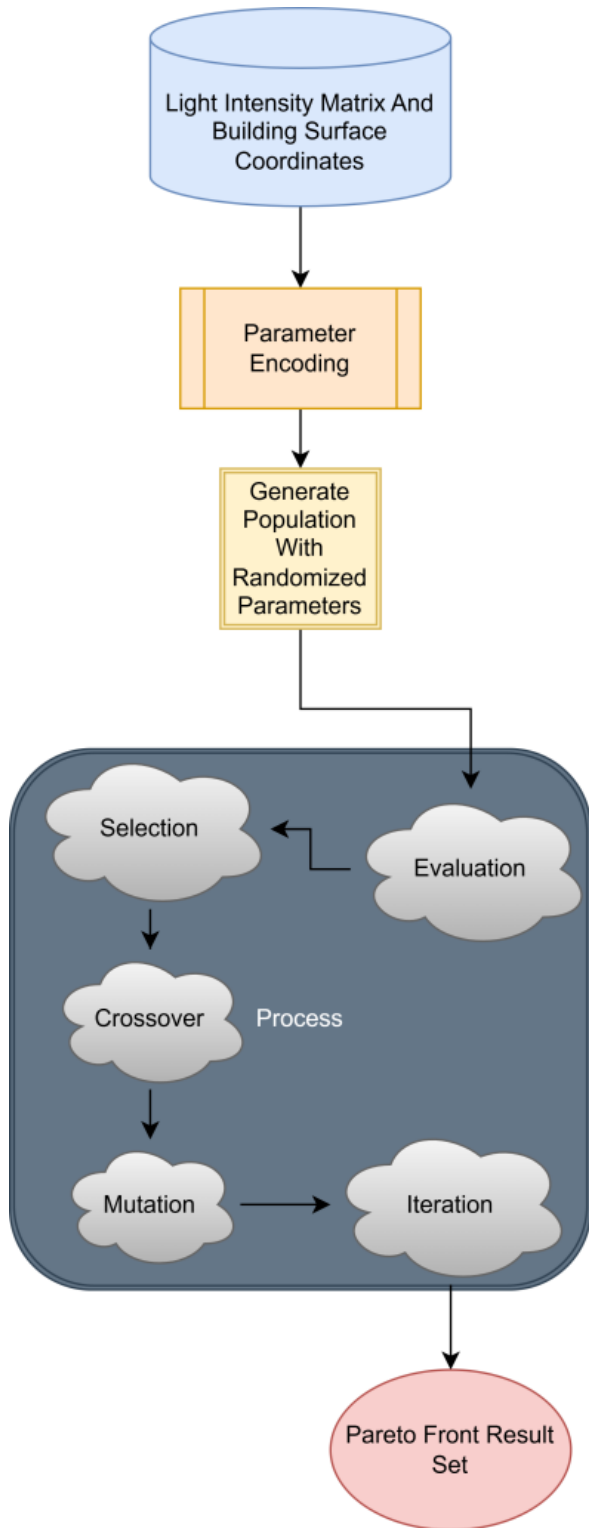


Fig. 2. Results of multi-objective optimization of photovoltaic module layout.

The algorithm takes the illuminance matrix and building surface coordinates as input, encodes the component tilt angle, azimuth angle, and spatial location as heritable variables, and randomly generates an initial layout scheme. Energy efficiency, reflection balance, and visual coherence are comprehensively evaluated through fitness calculations, and Pareto ranking and crowding distance are used to select

optimal solutions. Perturbations are introduced during crossover and mutation to maintain diversity. The algorithm iteratively balances energy performance and visual characteristics, ultimately outputting a Pareto front composed of high-efficiency and high-coherence solutions, revealing the multi-objective optimal distribution relationship of photovoltaic layout.

2.3. Visual Correction of Materials Based on Spectral Sensing Mapping

After conducting the spatial optimization of the energy and aesthetics synergies, performing spectral perception mapping on the material reflection spectrum to achieve synergy correction of brightness and chromaticity. The reflection curve is re-represented in visual space after nonlinear mapping and perception weighting to mitigate glare and chromaticity misalignment due to high contrast. The spectral perception mapping module takes the optimized component parameters and material reflection spectrum as input data, and adjusts the reflection and transmission coefficients of different bands through a nonlinear spectral mapping function to balance brightness distribution and color saturation [35]. This process is based on the visual response function to weight the energy reflectance of the material in the visible light region, and establishes the correspondence between spectral power distribution and human visual sensitivity. Optical realizations involve multi-layer interference coatings or colored encapsulants. These material treatments introduce a five percent efficiency penalty while achieving visual harmony. Each spectral channel in the illumination matrix is weighted to reduce the glare effect in the high contrast area of the surface and enhance color coordination, forming a corrected spectral perception model. Its calculation expression is shown in equation (6):

$$S'(\lambda) = a \cdot S(\lambda)^\gamma + b \tag{6}$$

$S'(\lambda)$ is the mapped spectral reflectance value; $S(\lambda)$ is the original spectral reflectance curve; γ is the nonlinear adjustment index used to control the degree of compression of reflected brightness, and a and b are the spectral intensity calibration coefficient and brightness offset term, respectively. Through this transformation, the highlight region of the material is smoothed, while the low-brightness part is enhanced, making the overall illumination level more balanced.

After the mapping is completed, the reflection spectrum is converted into luminance and chromaticity components using the spectral-to-visual-space mapping matrix. The luminance difference and color balance index are calculated using the CIE visual model of the International Commission on Illumination [36]. The visual consistency score is calculated by the variance ratio of the luminance and chromaticity gradient distributions and is used to measure the visual smoothness of the corrected surface. For the correction process of the visual attributes of photovoltaic surfaces, a nonlinear mapping function is applied in the spectral domain to dynamically adjust the reflection and transmission bands. The parameter configuration and weight allocation are shown in Table 2.

Table 2. Key Parameter settings for spectral mapping and visual correction model

Parameter Category	Parameter Name	Value / Range	Description
Spectral Mapping Function	Peak Reflectance Adjustment	0.8–1.2	Adjusts the reflectance curve amplitude across the visible spectrum
	Wavelength Shift Coefficient	0.85–1.15	Controls the spectral translation of the reflectance peak
Perceptual Weighting	Brightness Weight Factor	0.35	Weight for the lightness component in color perception
	Saturation Weight Factor	0.25	Weight for chroma component in color balance
	Hue Weight Factor	0.40	Weight for hue component alignment
Visual Evaluation Metric	Color Difference Threshold	≤ 5.0	Maximum acceptable perceptual deviation
Output Feature	Visual Consistency Score	0–1	Quantitative evaluation of color coherence after correction

To correct for amplitude shift in the reflection curves of various materials - from high-reflectance metals to low-reflectance glass - an adjustment coefficient is applied to the peak reflectance. This remains in the range of 0.8-1.2. The wavelength shift coefficient is in the range of 0.85-1.15 to handle spectral drift, given the influence of multilayer coating interference. Weights for luminance, saturation, and hue measure 0.35, 0.25, and 0.40, respectively, to account for the human eye's sensitivity to luminance as well as to hue, while allowing sufficient color balance across different materials, regions, and environments. A color difference threshold of ≤5.0 is applied to manage visual errors, and an output consistency index of 0-1 is applied here to quantify the visual cohesion following luminance and chromaticity correction. In summary, this system of parameters achieves harmony between the spectral response of the materials and perceptual weighting, ultimately developing a physically coherent and visually steady spectral mapping system.

2.4. Energy-Aesthetic Integrated Performance Output Model

To build an energy-aesthetic integrated performance framework that considers power generation efficiency, visual harmony, and spectral balance, the outcomes of multi-objective optimization and material visual correction are embodied under a single assessment framework to produce multi-dimensional design decision indicators, and the output is a visualization result that fuses energy harvesting efficiency and aesthetic harmony. The inputs are the optimal parameter set and the result of the spectral perception mapping. These are standardized and weighted to produce an overall energy-aesthetic score function. Normalizing all the indicators to the interval of [0,1]. Its weighted fusion function is defined in formula (7):

$$F_c = \alpha \cdot E_n + \beta \cdot V_n + \gamma \cdot S_n \quad (7)$$

In equation (7), F_c represents the comprehensive energy efficiency score; E_n is the standardized power generation efficiency index; V_n is the visual coordination score; S_n is the

spectral balance index; α , β , and γ are weighting coefficients, satisfying $\alpha + \beta + \gamma = 1$. To further refine the influence of visual features in the comprehensive index, a local illumination consistency term C_l and a color distribution smoothness term C_s are defined, reflecting the balance of light intensity gradient on the component surface and the continuity of color space, respectively. The visual consistency score is expressed as a weighted combination, as shown in equation (8):

$$V_n = \delta_1 \cdot (1 - \sigma_L) + \delta_2 \cdot (1 - D_c) \quad (8)$$

In equation (8), σ_L is the standard deviation of the brightness distribution; D_c is the color difference distance; and δ_1 and δ_2 are the weighting coefficients of visual features. Lower σ_L and D_c indicate more uniform surface brightness and chromaticity, thus improving visual harmony. The energy efficiency part consists of the annual average power generation density and solar utilization rate, and its standardized form is shown in equation (9):

$$E_n = \frac{E - E_{\min}}{E_{\max} - E_{\min}} \quad (9)$$

In equation (9), E_{\min} and E_{\max} represent the minimum and maximum power values in the sample set, respectively. The spectral balance index S_n is calculated based on the smoothness of the reflectance spectrum distribution and the spectral energy concentration, and its form is shown in equation (10):

$$S_n = 1 - \frac{\sum_{\lambda} |S'(\lambda + \Delta\lambda) - S'(\lambda)|}{\sum_{\lambda} S'(\lambda)} \quad (10)$$

In equation (10), $S'(\lambda)$ is the reflectance value after spectral sensing mapping, and $\Delta\lambda$ is the wavelength interval. A higher S_n value indicates that the material's reflectance spectrum changes smoothly across bands, resulting in higher optical consistency and helping to improve overall aesthetic harmony.

3. Experiment

3.1. Experimental Environment and Dataset Description

In order to validate the algorithms based on dynamic light energy mapping, multi-objective optimization, and spectral correction, the experiment was carried out in a high-end computing environment. The 0.5 m resolution 3D city model represented building morphology generated by merging GIS data and UAV point clouds; The study area is located at 113.23 degrees East and 23.16 degrees North. The climate type is humid subtropical. Data sources consist of 2024 meteorological station records and high-fidelity 3D urban geometries. Thus, the model was complete with building

facades, roofs, and shading. Illumination data were derived from a solar radiation monitoring program during 2024, at a one-hour sampling interval over the annual sun-cycle. Environmental parameters that were set in all simulations were a standard atmospheric model for mid-latitudes with an albedo of 0.23 and an atmospheric transmittance of 0.78. The computer science hardware was composed of an Intel Xeon Platinum 8380 CPU (Central Processing Unit), an NVIDIA A100 GPU (Graphics Processing Unit) (40 GB), 512 GB of RAM memory, and an Ubuntu 22.04 system. The code and algorithms were implemented in the Python programming language. The geometry models and illumination simulations were done here in Rhino-Grasshopper. Radiance engine was the tool that was used to perform radiative transfer calculations. The code utilizes parallel processing via CUDA to accelerate the multi-objective genetic algorithm iterations. The hardware configuration is detailed in Table 3.

Table 3. Experimental environment and equipment configuration

Category	Specification	Description
Central Processing Unit (CPU)	Intel Xeon Platinum 8380, 40 Cores, 2.3 GHz	Provides high parallel computing capability for illumination and optimization tasks
Graphics Processing Unit (GPU)	NVIDIA A100, 40 GB VRAM	Accelerates deep learning operations and rendering computations
Memory	512 GB DDR4	Supports large-scale 3D model processing and time-series data computation
Operating System	Ubuntu 22.04 LTS	Ensures system stability and compatibility for high-performance computing
Software Tools	Python 3.11, Rhino-Grasshopper, Radiance	Provides an integrated environment for modeling, simulation, and illumination analysis
Simulation Resolution	0.5 m Spatial Grid	Defines spatial precision of the city model, balancing detail and computational load
Radiation Sampling Interval	1 h	Specifies the temporal sampling frequency to capture the diurnal variation of solar radiation
Atmospheric Reflectivity	0.23	Represents surface and building reflectance, influencing light distribution
Atmospheric Transmittance	0.78	Describes atmospheric transparency affecting solar radiation attenuation

The parallel approaches for radiative transfer and genetic optimization were made possible by the Intel Xeon Platinum 8380 processor, which has 40 cores and a base frequency of 2.3 GHz. Large-scale matrices and spectral mappings are efficiently computed by the NVIDIA A100 graphics card, which has 40GB of video memory. Continuity of data and simulation in space, at a spatial resolution of 0.5 m, is ensured by the processor's 512 GB of DDR4 system memory. The combination of Ubuntu 22.04 LTS and Python 3.11 per library provides a productive and manageable manner for algorithm training iterations. An atmospheric albedo of 0.23 and broadband transmittance of 0.78 were derived from a mid-latitude urban radiation model to characterize energy loss and scattering from building surfaces. Radiance and Rhino-Grasshopper guarantee the truth and physical consistency of

the lighting simulation. The entire configuration thus constitutes a high-fidelity and stable experimental environment with the technical capability for photovoltaic integration optimization and visual modeling.

3.2. Experimental Procedure and Parameter Settings

The experimental methodology included illumination modeling, algorithm enhancement, and spectral correction to keep data continuity and computing rigor. It was initiated by bringing a 3D city model from Rhino-Grasshopper into Python, where the data were normalized. Illumination modeling was performed in Radiance; it simulated the radiation for an entire year with a 1-hour resolution. This stage resulted in an illumination matrix, which was processed

according to the multi-objective genetic algorithm (MOGA) approach. By means of the genetic algorithm, the optimization of the tilt angle, the azimuth angle, and the placement of components was done over a search period of 500 generations, and a population size of 200 was used. The Pareto criterion and crowding distance were employed to keep the diversity during the natural selection process. The weights for the components of the fitness function were $\alpha=0.45$, $\beta=0.35$, and $\gamma=0.20$, and the best parameters were chosen from the non-dominated solutions. In the spectral mapping operations, the

reflectance curves were adjusted and smoothed with a Gaussian kernel having $\Delta\lambda=5$ nm. The standardized luminance and chromaticity matrices were the results. During the visualizations phase, a 3D graph showing power generation, intensity of reflectance, and visual consistency was rendered out within Rhino. The entire process was rendered, parallel with breath, using CODA, and delivered in a unified hardware environment to ensure continuity across each stage of development and to synchronize data. Key parameters and resultant data are delineated in Table 4.

Table 4. Experimental parameter settings and model operation statistics

Parameter Type	Parameter Name	Value	Description
Algorithm Parameter	Population Size	200	Number of individuals per generation
Algorithm Parameter	Iterations	500	Total evolutionary steps in MOGA
Weight Coefficient	α	0.45	Energy efficiency weight
Weight Coefficient	β	0.35	Visual uniformity weight
Weight Coefficient	γ	0.20	Spectral smoothness weight
Spectral Mapping	Step Interval $\Delta\lambda$	5 nm	Sampling resolution in spectral fitting
Simulation Setting	Time Step	1 h	Temporal interval of radiation input
Computation	Average Runtime	7.8 h	Total computation time per full iteration
Computation	GPU Utilization	91%	Parallel acceleration efficiency

A population size of 200 and 500 iterations was utilized to ensure sufficient coverage of the solution space and reduce non-dominated solution shift with sampling size. The weighting coefficients $\alpha=0.45$, $\beta=0.35$, and $\gamma=0.20$ emphasized power generation efficiency but included visual balance and spectral smoothness in order to maintain multidimensional performance balance. A spectral fitting step size of $\Delta\lambda=5$ nm helped to balance the accuracy of sampling and prevent brightness drift, as a radiation simulation step size of 1 h provided temporal resolution on the yearly illumination distribution. On average, the seven parallel computations were completed in 7.8 hours, which corresponds to a parallel GPU utilization of 91%. The crossover and mutation operations were batched on tensor units while maintaining uniform computational stability, and thus, this parameter setting can be considered as a good compromise between accuracy, convergence speed, and spectral continuity in this context.

4. Results and Analysis

4.1. Analysis of Light Energy Harvesting Performance

To evaluate the performance of solar energy harvesting for the purpose of determining the radiation characteristics of building surfaces based on different orientations, the experiment combined the annual solar radiation time-series data, which was based on the irradiance modeling results. This was done to obtain the annual average irradiance and the effective radiation duration for each surface orientation. A baseline configuration using fixed thirty-degree tilt modules provides a reference point. The proposed method achieves a fifteen percent energy gain over the standard layout. The radiance computation results were compiled and standardized under typical meteorological conditions to create an annual solar energy density matrix. The whole procedure here distinguishes the variations in energy flux between the facade and the roof at the annual level and also computes the relative energy ratios to confirm the spatial accuracy and the directional response of the model performance. The statistical visualization outcomes generate a comparative map of the annual average solar energy density of each surface orientation, as depicted in Fig. 3.

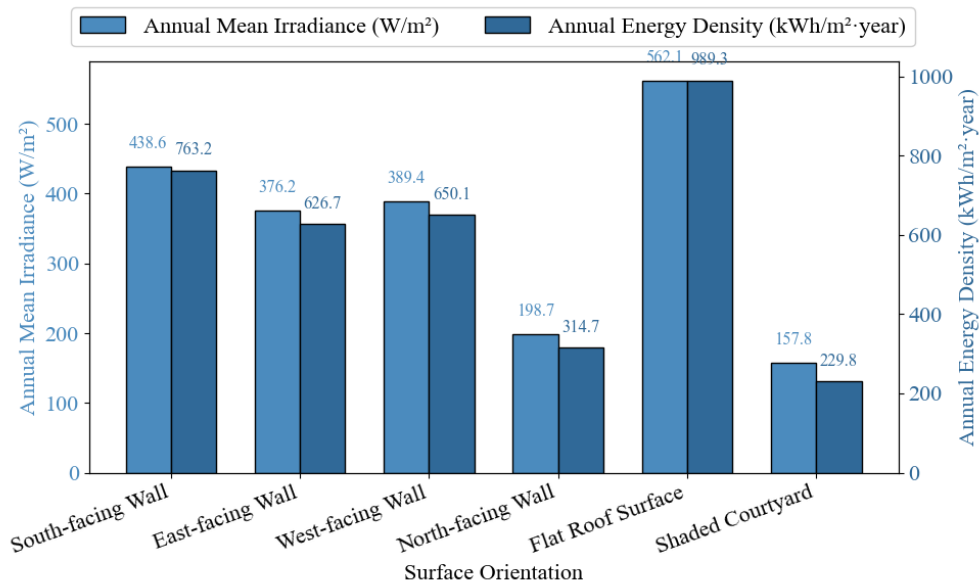


Fig. 3. Comparison of annual average solar energy density on building surfaces with different orientations.

The roof captures around 562.1 W/m² of solar radiation on average throughout the year, which corresponds to an annual energy density of 989.3 kWh/(m²·year). Besides unobstructed direct sunlight, the south-facing facade receives solar radiation of 438.6 W/m², which results in an energy density of 763.2 kWh/(m²·year). The value depends on the solar incidence angle and the peak hours of the day that are exposed to the sun throughout the year. Annual average irradiance represents the mean value during sunlit hours. The conversion to annual energy density utilizes the summation of hourly intervals multiplied by the system performance coefficient. Total equivalent sunlit hours for the south facade reach 1740 hours. The average solar radiation for the east and west-facing facades is 376.2 W/m² and 389.4 W/m², respectively, with energy densities of 626.7 kWh/(m²·year) and 650.1 kWh/(m²·year). Since the radiation peaks are distributed asymmetrically in the morning and evening, the total energy is at a moderate level. The north-facing facade that is heavily influenced by the backlighting and diffuse radiation in the long term, has its average irradiance going down to 198.7 W/m² with an annual energy density of only 314.7 kWh/(m²·year). The shaded courtyard is situated in a light-degraded environment between the multi-story buildings and shows an average irradiance of 157.8 W/m² and an energy density of 229.8 kWh/(m²·year); hence, there is major energy

loss. The overall results reveal that the light energy reception characteristics of building surfaces depend on incident angle, shading ratio, and spatial orientation, which are the combined factors. Photovoltaic integration design should focus on the roof and south-facing areas as the main deployment locations to build a high-energy base with effective radiation contributions.

To obtain the temporal radiation distribution characteristics of building surfaces facing different directions, the experiment was based on the radiative transfer simulation results under typical sunny conditions throughout the year. Hourly sampling and spatial weighted averaging of solar intensity were performed from 06:00 to 20:00. The model, based on the illumination matrix calculated by Radiance, dynamically tracks the incident radiation on each facade and roof at different solar altitude angles, incorporating building shading effects and diffuse components for correction, thus forming a complete temporal distribution curve of light energy. In the data processing stage, the light flux at each time step was weighted according to a spatial grid and output as a temporal sequence to characterize the response of different orientations to changes in solar angle. The results obtained after multi-time-segment integration are shown in Fig. 4.

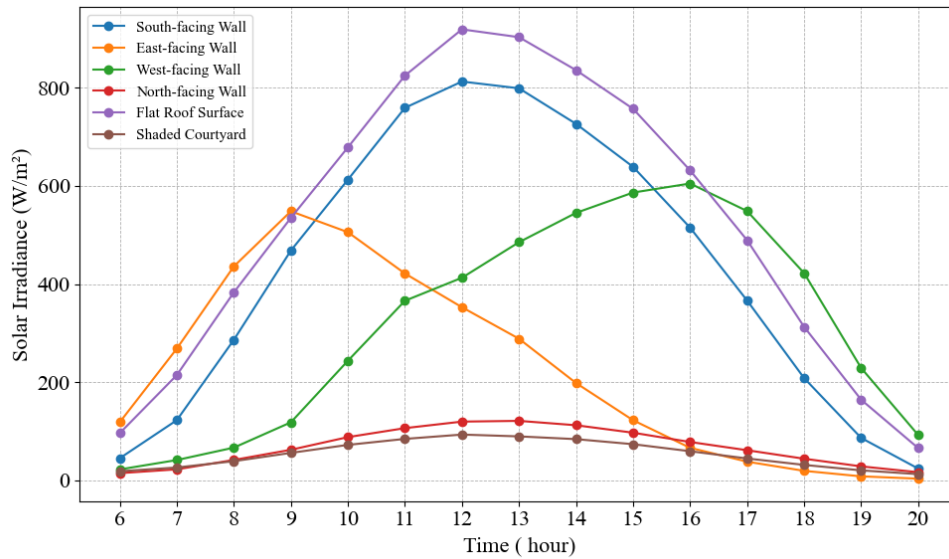


Fig. 4. Time-series variation curves of light intensity on building surface at different time periods.

The roof surface reached its peak irradiance of 918.7 W/m² at 12:00 PM, exhibiting the highest radiation reception due to its unobstructed location and near-perpendicular incident angle to the direction of solar radiation. The south-facing facade reached 812.4 W/m² at noon, maintaining a high irradiance level between 10:00 AM and 2:00 PM due to the sun's orbital tilt. The east-facing facade reached 435.8 W/m² at 8:00 AM and gradually decreased, with an earlier peak due to the concentrated angle of morning sunlight. The west-facing facade reached 604.7 W/m² at 4:00 PM, showing a clear afternoon radiation enhancement characteristic, mainly caused by the matching incident angle when the sun is setting in the west. The facade that faced the north side had its highest value of 121.3 W/m² at 1:00 PM when most of the radiation came from diffuse and reflected radiation. At 12:00 PM, the courtyard area had a maximum value of 93.4 W/m², which was influenced by the combined effects of ground surface and building reflections. The overall distribution features firstly show that the temporal differences of solar energy acquisition on building surfaces are mainly controlled by the solar azimuth angle and shading conditions. The south-facing and

roof areas, which absorb the most energy, are the main sources of key temporal data for the photovoltaic module deployment.

4.2. Analysis of Surface Illumination Distribution Uniformity

In order to check how evenly the light intensity was spread over the building surfaces in real lighting situations, an experiment implemented a radiative transfer model for spatial gridding sampling of the four walls facing south, east, west, and north, together with the roof area. By dividing the facade surface into 5×5 sampling units, the standard deviation and average illuminance of each grid were normalized, and the illuminance uniformity index of each unit was calculated to reflect the balance of local light distribution. The experiment kept the incident radiation energy, solar altitude angle, and meteorological parameters constant, only changing the orientation and structural shading characteristics of the building surface to obtain the uniformity variation of light in the spatial dimension. The resulting thermal results of the spatial distribution of illuminance uniformity on the building facade and roof are shown in Fig. 5.

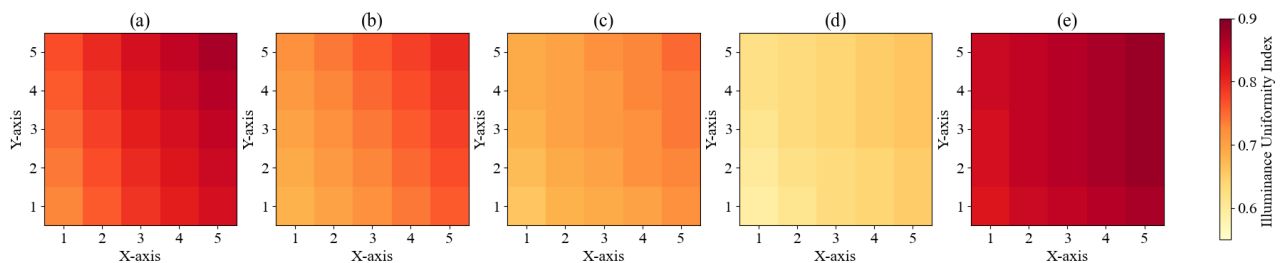


Fig. 5. Spatial heat map of uniformity of light illumination on building surface; (a). Uniformity of illumination on the south-facing façade; (b). Uniformity of illumination on the east-facing façade; (c). Uniformity of illumination on the west-facing façade; (d). Distribution of uniformity of illumination on the north-facing façade; (e). Uniformity of illumination on the roof surface.

The spatial uniformity of illuminance on the south-facing walls is fairly stable, with a uniformity index of at least 0.73

and at most 0.87, indicating that direct sunlight was more likely to yield a gradual illuminance gradient at upper angles

to the horizon. The roof area had the highest overall uniformity, with a uniformity index of 0.82 to 0.88 due to the unobstructed planar structure that distributes irradiance more uniformly across a horizontal plane. East-west facades ranged from 0.66 to 0.80 uniformity indices, indicating large variations mostly related to changes in angle of incidence at dawn and dusk and reflected light returning from other structures. The north-facing walls were generally two-dimensional conditions of indirect light with uniformity indices of mostly 0.59 to 0.66, indicating that shadow shading noticeably interrupted illuminance distributions. For the most part, the trend identified was that illumination uniformity is closely related to orientation, reflection conditions, and shading geometry, meaning the south-facing facades and roof had better spatial light field uniformities under pronounced stable irradiance conditions.

4.3. Visual Harmony and Color Balance Analysis

To evaluate the visual consistency effect of the model on different photovoltaic material surfaces, a visual consistency index was constructed based on experimental reflectance spectral data to compare material types and visual consistency before and after spectral mapping. Five typical materials—monocrystalline silicon, polycrystalline silicon, thin-film silicon, perovskite, and coated photovoltaic glass—were selected, and the visual consistency score (VCS) before and after mapping was calculated to quantify the impact of spectral adjustment on color balance and brightness coordination. Through nonlinear spectral perception mapping, the material reflectance characteristics were matched with the human visual response, and the VCS change trend before and after spectral correction for each material was obtained, as shown in Fig. 6.

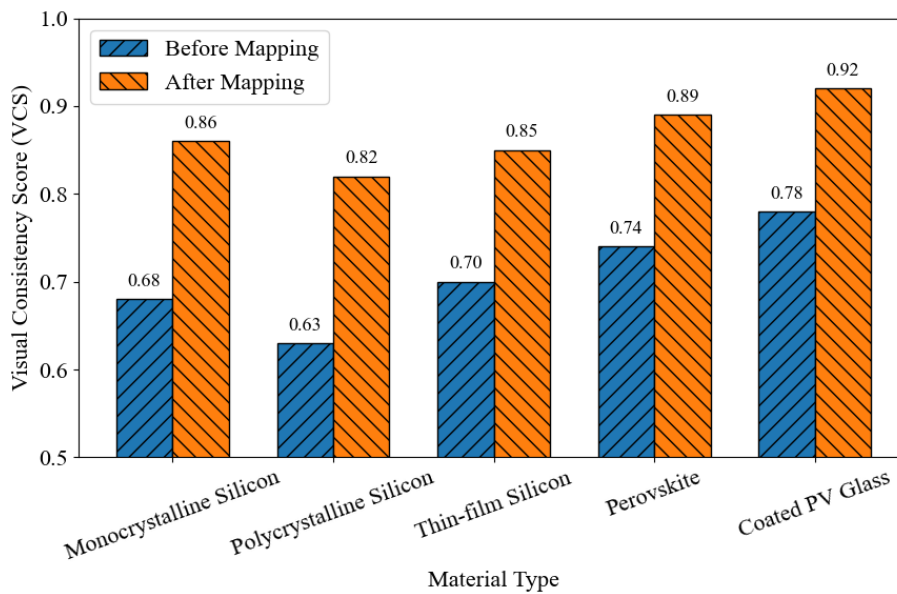


Fig. 6. Comparison of visual consistency indices of different material surfaces.

The visual consistency score (VCS) of monocrystalline silicon was improved from 0.68 to 0.86, as a result of improved alignment of the narrowband reflection peak with the visible light-sensitive band, which effectively decreased statistically significant brightness fluctuations occurring at higher frequencies. The VCS of polycrystalline silicon was elevated to 0.82 after the mapping was performed; the original reflection was biased toward a strong directional pattern for reflection, and the mapping algorithm smoothed the distribution of reflection across the surface. The VCS of thin-film silicon was elevated to 0.85, indicative of the suppressive effects of a broadband absorption structure on color-shifting processes related to spectrum-mapped modeling. The VCS for perovskite materials increased from 0.74 to 0.89, due to its high degree of spectral correspondence within the 400 - 700 nm range, as the color shift was reduced in portions of the spectra that exhibited enhanced brightness. The VCS for composite coated glass reached 0.92, as a result of its multilayer film structure suppressing the heterogeneous distribution of reflected energy following the mapping model.

Overall, the outcomes indicate that the spectral mapping model successfully decreased color shifting and enhanced visual consistency for different types of photovoltaic materials by modifying the band resonance characteristics within the material surfaces.

In the spectral correction stage, visual consistency mapping based on the CIE Lab color space was further conducted on the photovoltaic surface after multi-objective optimization to analyze the brightness and chromaticity distribution patterns of different regions after correction. The experiment involved calculating the L^* , a^* , and b^* parameters point-by-point for nine regions across the upper, middle, and lower layers. From these values, the color differences of each region relative to the center point were derived. The results were visualized as a thermal distribution to reveal the influence of local illumination, reflection, and incident angle variations on surface color uniformity. After color space interpolation and normalization, a thermal map of the

corrected surface color space distribution was generated, as shown in Fig. 7.

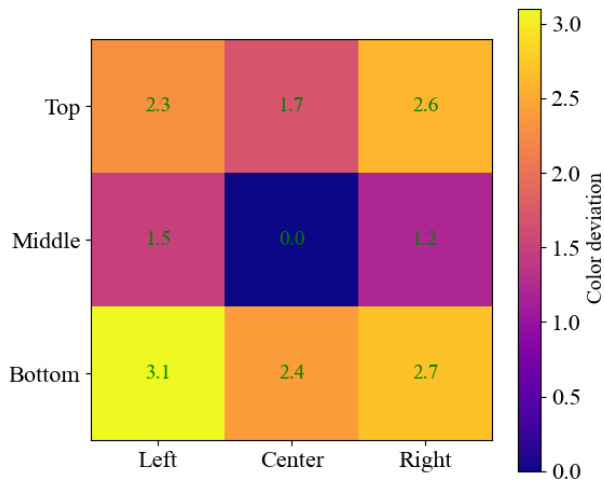


Fig. 7. Thermal diagram of surface color space distribution.

The center region demonstrates the 0.0 color difference, indicating the optimal spectral distribution. The upper-middle section displays a 1.7 color difference, showcasing the bright, cool color explained by the aggregation of light that features significant reflection. The right-middle region has a color

difference of 1.2, consistent with a fairly uniform horizontal distribution. The lower-left region indicates a 3.1 color difference due to the decrease of radiant flux approaching the decreasing incident angle; therefore, it is less affected by the original color with less light. The upper-right segment indicated a color difference of 2.6, which may also be attributed to the reduction of reflection strength derived from local shading of other things. Overall, there is a progression of vertical color difference with a decrease in incident angle, suggesting that the direction of light influence and the geometric reflection can impact the color balance. The correction model demonstrates the best spectral characteristics consistency in the center of the overall area.

4.4. Comprehensive Assessment of Energy-aesthetic Coupling

To evaluate the overall coordination between energy performance and visual appeal of photovoltaic systems, an energy-aesthetic coupling characteristic analysis based on multidimensional indices was conducted. Standardized analyses were performed on samples of monocrystalline silicon, polycrystalline silicon, thin-film silicon, perovskite, and composite-coated glass. A multidimensional performance mapping model was established using a normalized index matrix to visualize the synergistic performance of multiple properties for each material. The results are shown in Fig. 8.

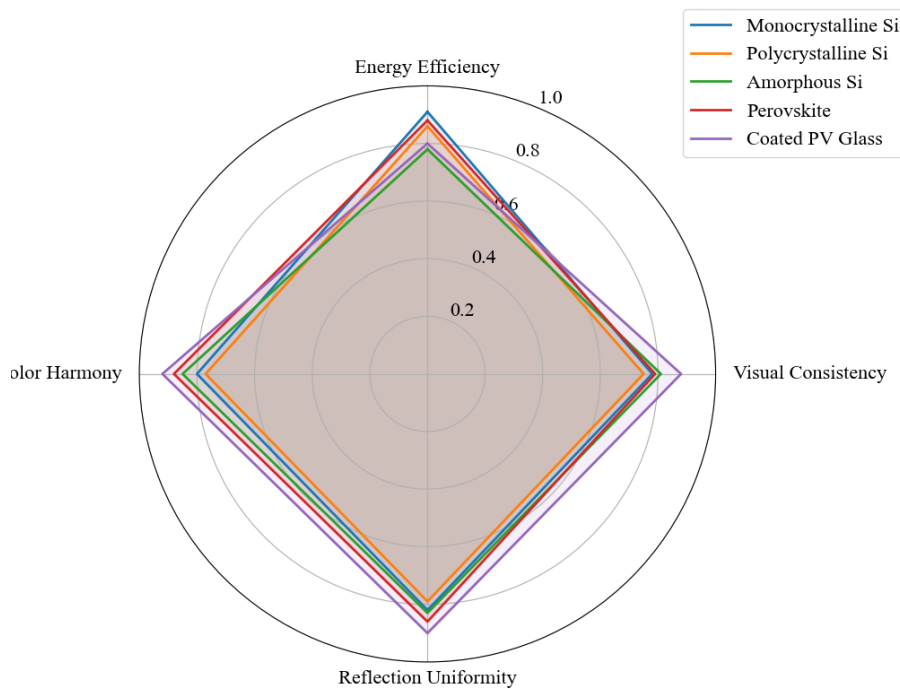


Fig. 8. Radar diagram of the overall coupling degree.

Monocrystalline silicon attained an energy efficiency of 0.91, demonstrating a high energy efficiency level from its high photoelectric conversion stemming from its crystal structure and short carrier migration distance. Composite

coated glass has a color harmony and visual consistency reading of 0.92, while its high reflectance uniformity index of 0.88 is attributed to the control of the visible spectrum from the multi-layer surface coating and more visually uniform

layers. Perovskite materials produced an energy efficiency of 0.88 while also providing a color harmony of 0.88, meaning the absorption layer thickness and interface transparency were optimized to balance energy absorption and visual reflection. Thin-film silicon is low with an energy efficiency of only 0.78; however, the diffuse reflection properties of thin-film silicon allow for a higher reflectance uniformity and color harmony, which were measured at 0.81 and 0.85, respectively. Polycrystalline silicon is a relatively balanced energy and visual performance material, although it is slightly dispersed due to grain boundary scattering and surface roughness.

4.5. Model Robustness and Urban Adaptability Analysis

Under different weather conditions, the stability of the model output is jointly affected by light intensity, ambient

humidity, and light scattering characteristics. This section constructs standardized experimental scenarios to statistically analyze the output stability of the model under five weather conditions: sunny, cloudy, overcast, rainy, and hazy. Sky conditions are parameterized using the Perez All-Weather Sky Model. DNI and DHI distributions follow the turbidity factors and transmittance values of each climate class. The minimum, quartiles, median, and maximum values are calculated to reflect the differences in the model's response under different external light and climate disturbances. The experiments are conducted under constant input parameters and consistent spectral sampling conditions to ensure that the results are only affected by weather variables. Based on the obtained data, a box plot of output stability is plotted to visually demonstrate the discreteness and central tendency distribution of the model's response under diverse weather conditions, as shown in Fig. 9.

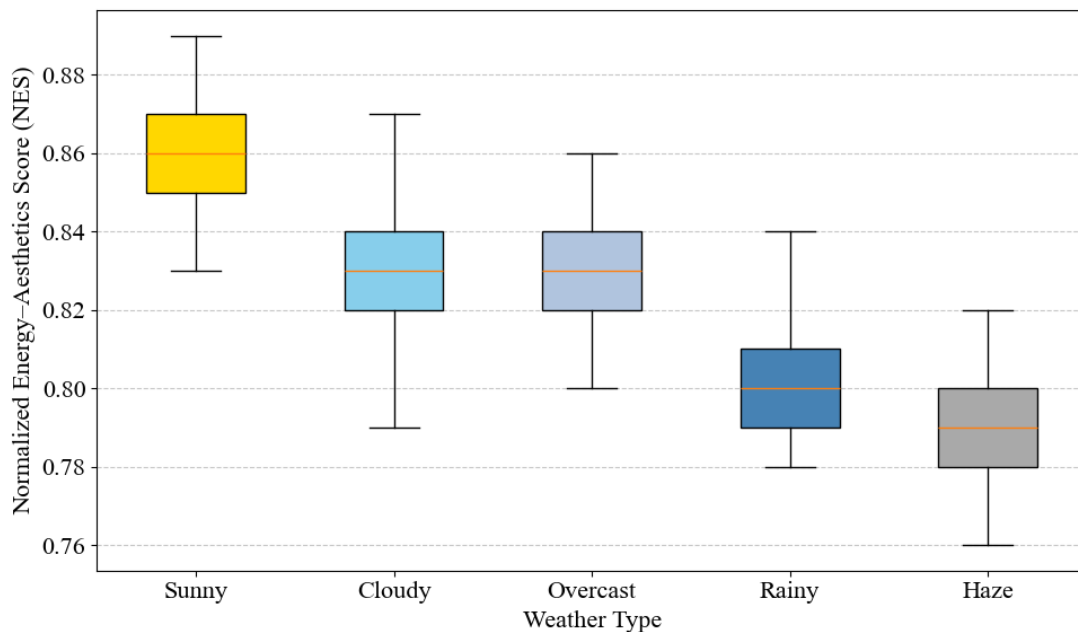


Fig. 9. Box plot of output stability under different weather conditions.

Using bright sunshine conditions, the median NES output was 0.86, which was the most stable for all weather conditions. The stability was mainly due to abundant direct sunlight and a consistent spectral distribution, promoting high stability in the model's fit between energy and visual response. The median for cloudy and overcast days was 0.83; while the median was lower than sunny conditions, the cloudy and overcast days had a higher proportion of diffuse light, which has less local reflection and, therefore, made the model fit more uniform. The model median decreased with rainy conditions to 0.80, where the increased humidity caused changes to surface reflectance and nonlinear intensity fluctuations. The median for hazy conditions was 0.79 and was the least stable NES output. The stability was the least due to aerosol particles elongating the scattering path for light dissipation, which continued to make the model's intensity estimates deviate from the true brightness. Overall, the established stability of the model's output diminishes as atmospheric transparency decreases,

demonstrating the interference of light scattering and reflection to be key components for stability inhibition in energy output.

5. Conclusion

This paper presents a Photovoltaic Aesthetic Integration Design Method (PAIDM) based on dynamic light energy mapping and multi-objective optimization, achieving synergistic optimization of energy harvesting and visual performance of photovoltaic systems in urban built environments. This research develops a spatial distribution matrix of irradiance, utilizing a radiative transfer model, and uses a multi-objective genetic algorithm to maximize simultaneously the tilt angle, azimuth angle, and mounting location of photovoltaic modules to achieve a global compromise between power generation performance, uniformity of reflectivity, and aesthetic coherence. Additionally, a spectral sensing mapping function was

utilized to non-linearly adjust the reflectivity behavior of the material, resulting in improved brightness distribution and color harmony. Resulting from the experiment, an average yearly solar radiation of the south-facing facade is leading to 438.6 W/m², which translates to a solar energy density of 763.2 kWh/(m²·year). The visual consistency score of the adjusted monocrystalline silicon material has risen from 0.68 to 0.86. The median performance stability of the model was over 0.78 under different weather conditions, thus the algorithm is quite robust in complex lighting. Subsequent research phases entail the physical deployment of sensor-equipped photovoltaic prototypes on actual urban building facades to measure the deviations between the numerical model and physical energy yields. This study has redesigned the structural transition of photovoltaic systems, where they no longer serve as functional components but become aesthetic features, thus enabling a dynamic balance of energy harvesting performance and visual communication over building facades. In addition to that, the research provides a route for the harmonious coupling of energy performance and aesthetic value in the context of urban environmental design. Urban planners and architectural engineers serve as the primary beneficiaries of this framework, utilizing the numerical outputs for district-level renewable energy planning and facade material selection. The current algorithm exhibits high computational efficiency at the single-building scale, demanding further parallel processing optimizations to accommodate city-wide geometric datasets without memory saturation.

Acknowledgement

N/A

Authorship Contribution Statement

Guangyu YANG: Writing-Original draft preparation, Conceptualization, Supervision, Project administration.

Shilong XU: Methodology, Software, Validation.

Conflicts of Interest

The authors declare that there is no conflict of interest regarding the publication of this paper.

Declaration of generative AI

During the preparation of this work the authors used Chat GPT, version 4 in order to language editing and improving readability. After using this tool/service, the authors reviewed and edited the content as needed and take full responsibility for the content of the published article.

References

- [1] D. J. Sailor, J. Anand, and R. R. King, "Photovoltaics in the built environment: a critical review," *Energy and Buildings*, vol. 253, p. 111479, 2021.
- [2] Y. Lu, M. Chen, G. Zhu, and Y. Zhang, "Recent progress in the study of integrated solar cell-energy storage systems," *Nanoscale*, vol. 16, no. 18, pp. 8778-8790, 2024.
- [3] S. Constantinou, F. Al-Naemi, H. Alrashidi, T. Mallick, and W. Issa, "A review on technological and urban sustainability perspectives of advanced building-integrated photovoltaics," *Energy Science & Engineering*, vol. 12, no. 3, pp. 1265-1293, 2024.
- [4] M. S. Rajan, "Optimizing photovoltaic panel performance: a comparative study of meta-heuristic algorithms," *Advances in Engineering and Intelligence Systems*, vol. 3, no. 2, pp. 83-105, 2024.
- [5] J. Marchwiński, "Research on BIPV in office and public utility buildings in aesthetic and utility context," *Sustainability*, vol. 15, no. 1, p. 136, 2022.
- [6] G. Wang, "Performance evaluation and optimization of photovoltaic systems in urban environments," *International Journal of New Developments in Engineering and Society*, vol. 9, pp. 42-49, 2025.
- [7] E. Lucchi, J. Adami, and A. E. Stawinoga, "Social acceptance of photovoltaic systems in heritage buildings and landscapes: exploring barriers, benefits, drivers, and challenges for technical stakeholders in northern Italy," *Sustainable Energy Technologies and Assessments*, vol. 60, p. 103544, 2023.
- [8] Y. Huang, Y. Yang, H. Ren, L. Ye, and Q. Liu, "From urban design to energy sustainability: how urban morphology influences photovoltaic system performance," *Sustainability*, vol. 16, no. 16, p. 7193, 2024.
- [9] C. Li, W. Zhang, F. Liu, X. Li, J. Wang, and C. Li, "Multi-objective optimization of bifacial photovoltaic sunshade: towards better optical, electrical and economical performance," *Sustainability*, vol. 16, no. 14, 2024.
- [10] S. Shi and N. Zhu, "Challenges and optimization of building-integrated photovoltaics (BIPV) windows: a review," *Sustainability*, vol. 15, no. 22, p. 15876, 2023.
- [11] N. Albinus, B. Rau, M. Riedel, and C. Ulbrich, "A comprehensive case study of a full-size BIPV facade," *Energies*, vol. 18, no. 5, p. 1293, 2025.
- [12] I. D. H. López and L. Olivieri, "Comprehensive review of building-integrated photovoltaics in the renovation of heritage buildings," *Journal of Building Engineering*, p. 112883, 2025.
- [13] S. N. Vodapally and M. H. Ali, "A comprehensive review of solar photovoltaic (PV) technologies, architecture, and its applications to improved efficiency," *Energies*, vol. 16, no. 1, p. 319, 2022.
- [14] N. Martín-Chivelet, G. Montero-Gómez, E. Lorenzo, M. Fernández, J. I. Arribas, and A. Hernández-Callejo, "Building-integrated photovoltaic (BIPV) products

- and systems: a review of energy-related behavior,” *Energy and Buildings*, vol. 262, p. 111998, 2022.
- [15] A. Rodrigues, A. C. Oliveira, and A. I. Palmero-Marrero, “Integration of PV systems into the urban environment: a review of their effects and energy models,” *Urban Science*, vol. 8, no. 4, p. 215, 2024.
- [16] N. Fahoum and M. Sitbon, “Effects of building color, material, and angle on bifacial and transparent solar panels,” *Processes*, vol. 13, no. 2, p. 480, 2025.
- [17] A. B. Block, A. Virtuani, J. E. Palou, A. Faes, and C. Ballif, “Colouring solutions for building integrated photovoltaic modules: a review,” *Energy and Buildings*, vol. 314, p. 114253, 2024.
- [18] J. E. Gonçalves, H. Montazeri, T. van Hooff, and D. Saelens, “Performance of building integrated photovoltaic facades: impact of exterior convective heat transfer,” *Applied Energy*, vol. 287, p. 116538, 2021.
- [19] M. K. Basher, M. Nur-E-Alam, M. M. Rahman, K. Alameh, and S. Hinckley, “Aesthetically appealing building integrated photovoltaic systems for net-zero energy buildings: current status, challenges, and future developments—a review,” *Buildings*, vol. 13, no. 4, p. 863, 2023.
- [20] A. Røyset, T. Kolås, Ø. Nordseth, and C. C. You, “Optical interference coatings for coloured building integrated photovoltaic modules: predicting and optimising visual properties and efficiency,” *Energy and Buildings*, vol. 298, p. 113517, 2023.
- [21] X. Qiao, T. Zhao, X. Zhang, and Y. Li, “Multi-objective optimization of building integrated photovoltaic windows in office building,” *Energy and Buildings*, vol. 318, p. 114459, 2024.
- [22] E. Noorzai, P. Bakmohammadi, and M. A. Garmaroudi, “Optimizing daylight, energy and occupant comfort performance of classrooms with photovoltaic integrated vertical shading devices,” *Architectural Engineering and Design Management*, vol. 19, no. 4, pp. 394-418, 2023.
- [23] H. M. Maghrabie, A. M. Abdelkader, M. A. El-Din, M. M. Hegazy, and A. M. Hamed, “State-of-the-art technologies for building-integrated photovoltaic systems,” *Buildings*, vol. 11, no. 9, p. 383, 2021.
- [24] A. Azami and H. Sevinç, “The energy performance of building integrated photovoltaics (BIPV) by determination of optimal building envelope,” *Building and Environment*, vol. 199, p. 107856, 2021.
- [25] A. Y. Khan, Z. Ahmad, T. Sultan, S. Alshahrani, K. Hayat, and M. Imran, “Optimization of photovoltaic panel array configurations to reduce lift force using genetic algorithm and CFD,” *Energies*, vol. 15, no. 24, p. 9580, 2022.
- [26] G. Espitia-Mesa, A. Moreno-Villa, S. Tobón-Echavarría, J. C. Rivera, and R. Mejía-Gutiérrez, “Modeling optimal PV surface of BIPVs for maximum energy yield through genetic algorithms,” *Energy and Built Environment*, vol. 6, no. 4, pp. 607-615, 2025.
- [27] M. Valinejadshoubi, A. K. Athienitis, A. Bagchi, and M. Abtahi, “Integrated dynamic photovoltaic facade for enhanced building comfort and energy efficiency,” *Biomimetics*, vol. 9, no. 8, p. 463, 2024.
- [28] G. Russo, L. Pompei, G. F. Giuzio, M. Ferrero, A. Rinaldi, and P. Salatino, “Modelling the complexity of interconnected energy systems at different urban scales: a critical review,” *Renewable and Sustainable Energy Reviews*, vol. 223, p. 116007, 2025.
- [29] N. Caglayan, H. K. Celik, F. Öktüren Asri, M. Yılmaz, and A. Kaya, “Experimental validation and performance benchmarking of a grid-connected rooftop photovoltaic system using measured and simulated data,” *Energies*, vol. 19, no. 6, p. 1468, 2026.
- [30] C. Caliot, R. Schoetter, V. Forest, V. Eymet, and T.-Y. Chung, “Model of spectral and directional radiative transfer in complex urban canopies with participating atmospheres,” *Boundary-Layer Meteorology*, vol. 186, no. 2, pp. 145-175, 2023.
- [31] R. Schoetter, R. J. Hogan, C. Caliot, and V. Masson, “Coupling the urban canopy model TEB (SURFEXv9.0) with the radiation model SPARTACUS-Urbanv0.6.1 for more realistic urban radiative exchange calculation,” *EGU sphere*, vol. 2024, pp. 1-33, 2024.
- [32] P. Kosmopoulos, D. K. Papanikolaou, A. N. Assimakopoulos, and M. Santamouris, “Ray-tracing modeling for urban photovoltaic energy planning and management,” *Applied Energy*, vol. 369, p. 123516, 2024.
- [33] N. H. F. Beebe, “A complete bibliography of publications in the *Journal of Mathematical Chemistry*,” 2024.
- [34] D. D’Agostino, F. Minelli, and F. Minichiello, “New genetic algorithm-based workflow for multi-objective optimization of net zero energy buildings integrating robustness assessment,” *Energy and Buildings*, vol. 284, p. 112841, 2023.
- [35] J. C. Ortiz Lizcano, M. A. Del Río, P. Contreras, A. Virtuani, and C. Ballif, “Optimal design of multilayer optical color filters for building-integrated photovoltaic (BIPV) applications,” *Solar RRL*, vol. 7, no. 19, p. 2300256, 2023.
- [36] A. B. Block, J. E. Palou, A. Faes, A. Virtuani, and C. Ballif, “Accurate color characterization of solar photovoltaic modules for building integration,” *Solar Energy*, vol. 267, p. 112227, 2024.